

Article

New Perspective on Planar Inductive Sensors: Radio-Frequency Refractometry for Highly Sensitive Quantification of Magnetic Nanoparticles

José Luis Marqués-Fernández ¹, María Salvador ¹, José Carlos Martínez-García ¹, Pablo Fernández-Miaja ², Alfredo García-Arribas ³ and Montserrat Rivas ^{1,*}

¹ Department of Physics & IUTA, University of Oviedo, Campus de Viesques, 33203 Gijón, Spain

² Department of Electrical Engineering, University of Oviedo, Campus de Viesques, 33203 Gijón, Spain

³ Department of Electricity and Electronics, University of the Basque Country, 48940 Leioa, Spain

* Correspondence: rivas@uniovi.es

Abstract: We demonstrate how resonant planar coils may be used as sensors to detect and quantify magnetic nanoparticles reliably. A coil's resonant frequency depends on the adjacent materials' magnetic permeability and electric permittivity. A small number of nanoparticles dispersed on a supporting matrix on top of a planar coil circuit may thus be quantified. Such nanoparticle detection has application detection to create new devices to assess biomedicine, food quality assurance, and environmental control challenges. We developed a mathematical model for the inductive sensor response at radio frequencies to obtain the nanoparticles' mass from the self-resonance frequency of the coil. In the model, the calibration parameters only depend on the refraction index of the material around the coil, not on the separate magnetic permeability and electric permittivity. The model compares favourably with three-dimensional electromagnetic simulations and independent experimental measurements. The sensor can be scaled and automated in portable devices to measure small quantities of nanoparticles at a low cost. The resonant sensor combined with the mathematical model is a significant improvement over simple inductive sensors, which operate at smaller frequencies and do not have the required sensitivity, and oscillator-based inductive sensors, which focus on just magnetic permeability.

Keywords: self-resonant frequency; inductive sensor; coil; nanoparticles; magnetic nanoparticles; magnetic lateral flow immunoassays; impedance; refraction index; magnetic permeability; electric permittivity



Citation: Marqués-Fernández, J.L.; Salvador, M.; Martínez-García, J.C.; Fernández-Miaja, P.; García-Arribas, A.; Rivas, M. New Perspective on Planar Inductive Sensors: Radio-Frequency Refractometry for Highly Sensitive Quantification of Magnetic Nanoparticles. *Sensors* **2023**, *23*, 2372. <https://doi.org/10.3390/s23052372>

Academic Editor: Càndid Reig

Received: 22 December 2022

Revised: 13 February 2023

Accepted: 16 February 2023

Published: 21 February 2023



Copyright: © 2023 by the authors. Licensee MDPI, Basel, Switzerland. This article is an open access article distributed under the terms and conditions of the Creative Commons Attribution (CC BY) license (<https://creativecommons.org/licenses/by/4.0/>).

1. Introduction

New sensors are needed to detect and quantify nanoparticles (NPs) for increasing new applications. One example is the detection of biomolecules (toxins, disease biomarkers, or others), which are selectively attached to the particles through an immunological reaction [1]. There are several approaches for it, such as immobilising the particle-labelled molecule onto the sensor surface, using microfluidics to take the sample to the sensor or to pass it over its sensitive part, or paper-based microfluidics [2,3]. The latter is well known for being the basis of the COVID-19 rapid diagnostic tests [4]. Such tests have two main limitations that hinder their wider application; one is the lack of sensitivity (many false-negative results), and the other is their unreliable quantification. To improve it, some authors rely on magnetic nanoparticles (MNPs) as labels [5–8], which can be detected by devices sensitive to the fringes of their magnetic field, as in [9]. New needs in life sciences, such as healthcare, food safety, and environmental control, require further improvement in the sensitivity and quantifying capabilities of MNP-detecting sensors due to the extremely small number of particles immobilised at the test line and their tiny size.

Previous works [10–12] highlighted the ability to detect and quantify small numbers of MNPs by monitoring the impedance changes in a planar coil at a fixed frequency in the order of tens of MHz. The sensor is sensitive to magnetic permeability variations around the planar coil [13] as a consequence of Faraday’s electromagnetic induction law and can be observed as changes in its impedance. The larger the frequency, the larger the impedance change, as long as we are below the coil’s resonance frequency. In general, reliably obtaining small impedance changes in the MHz range requires expensive equipment (such as impedance or vector-network analysers,) so lower-cost and portable solutions would be more accessible and better combined with the inexpensive LFIAAs.

Some reported miniaturised devices focus on cost reduction using oscillator-based inductive detectors, and their reported sensitivity is 3 Hz/ μg Fe₃O₄ [9,14]. Such sensitivity is not enough for the requirements of many new potential applications, such as toxin detection in foods or early diagnosis.

Based on the central idea of [14], in this work, we improved MNP detection sensitivity while keeping costs down using the sensor coils’ self-resonant frequency (SRF). The main roadblock of SRF-based detectors is the complexity of the mathematical relation between the SRF and MNPs’ mass. We solved this bottleneck as described in Section 2. A usable, easy-to-implement, and precise mathematical model to correlate the coils’ SRF and the nanoparticles’ mass (volume or number, depending on the variable used for the calibration) is indispensable to make this measurement technique viable. We developed such a targeted model and tested it against simulations and experimental results to verify its validity and explored its limitations. Even when the central purpose was to develop and test the mathematical model, our analysis revealed a significant sensitivity and signal-to-noise ratio increases.

2. Mathematical Fundamentals

The method we developed to quantify nanoparticles (NPs) involves a planar coil and monitoring its SRF for different NP masses (whether magnetic or not) placed on top of it. Generally, the sensors that detect metal particles use single- or multiple-turn planar coils [15]. Due to its electromagnetic-field uniformity, we used a two-turn coil for this work. The planar nature of the coil allows the placement of flat samples (as the LFIAAs) on top of the sensor for its measurement. Figure 1 illustrates a bi-dimensional projection of the coil shape.

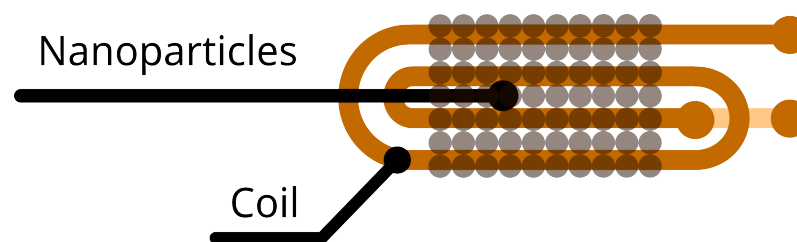


Figure 1. Representation of the sensing coil used in this work and sample placement.

The main goal of this section is to deduce a mathematical expression that relates the planar coil’s SRF and the NP mass on top of it. Using some hypotheses, we modelled this relationship in a simple and easy-to-use manner. The first simplifying hypothesis is to consider only the first SRF mode of our sensing coil, which allows us to model the coil’s impedance as an equivalent circuit. Using equivalent circuits to define the behaviour of transmission lines is a widespread and accepted procedure [16–19]. Simple inductors, such as those in Figure 1 are generally modelled using an inductor–capacitive network, as in Figure 2.

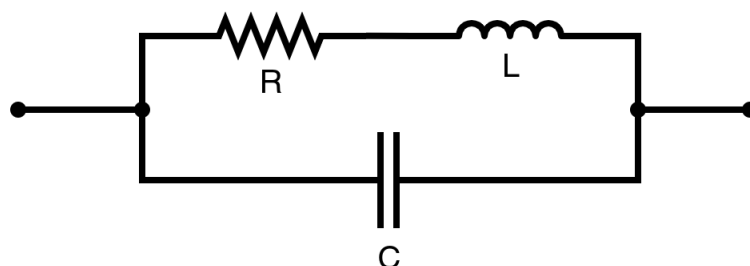


Figure 2. Equivalent circuit used to describe the behaviour of the inductor.

The model has been used before to approximate the core material properties of the coil [20], including complex magnetic permeability and electric permittivity as follows: way.

$$Z_L = \omega L i(\mu'_{\text{eff}} - i\mu''_{\text{eff}}) \quad (1)$$

$$Z_C = \frac{1}{\omega C i(\epsilon'_{\text{eff}} - i\epsilon''_{\text{eff}})} \quad (2)$$

$$Z_{\text{EQ}} = \left(\frac{1}{Z_L + Z_R} + \frac{1}{Z_C} \right)^{-1} \quad (3)$$

where Z_L stands for the inductive component, Z_C is the capacitive one, and $Z_R = R$ is the resistance of the equivalent circuit; ω is the operating angular frequency, L is the coil self-inductance, and C its capacitance; $(\mu'_{\text{eff}} - i\mu''_{\text{eff}})$ and $(\epsilon'_{\text{eff}} - i\epsilon''_{\text{eff}})$ are, respectively, the effective complex initial magnetic permeability and effective complex initial electric permittivity. Here, the term “effective” and the subindex “eff” refer to the effect of all the materials surrounding the coil. Equation (3) has some frequency-dependent parameters, such as the inductive and capacitive reactances, material properties (for example, the magnetic permeability is frequency-dependent, as established with the Néel or Brownian model, depending on the combination of material composition and size, magnetic-field intensity, and its frequency range), skin effects (which, being a consequence of Faraday’s induction, narrows the current path with increasing frequencies), and other non-linearities. Regardless, in the proximities of the SRF, NPs produce only minor variations in the frequency, so, in a first approximation, these variables can be taken as constants. The equivalent impedance model allows us to calculate the SFR as the first frequency value for which the impedance’s imaginary component vanishes. This approach has been previously used to characterise choke cores [21].

$$\text{SRF} = \frac{\sqrt{LC \epsilon'_{\text{eff}} \mu'_{\text{eff}}{}^3 - C^2 Z_R^2 \epsilon'_{\text{eff}}{}^2 \mu'_{\text{eff}}{}^2 + LC \epsilon'_{\text{eff}} \mu'_{\text{eff}}{}^2 \mu''_{\text{eff}}{}^2 - C Z_R \epsilon'_{\text{eff}} \mu'_{\text{eff}} \mu''_{\text{eff}}}}{2\pi C L \epsilon'_{\text{eff}} \mu'_{\text{eff}}{}^2 + 2\pi L C \epsilon'_{\text{eff}} \mu''_{\text{eff}}{}^2} \quad (4)$$

Given that, in general, the number of NPs to quantify is meagre, we expect that $\mu''_{\text{eff}} \approx 0$. In any case, the numerical simulations prove this assumption to be acceptable. For our coil geometry, $C^2 Z_R^2$ is much smaller than LC so that the expression of the SRF can be simplified to

$$\text{SRF} = \frac{\sqrt{LC \epsilon'_{\text{eff}} \mu'_{\text{eff}}{}^3}}{2\pi L C \epsilon'_{\text{eff}} \mu'_{\text{eff}}{}^2} = \frac{1}{2\pi \sqrt{LC \mu'_{\text{eff}} \epsilon'_{\text{eff}}}} = \frac{1}{2\pi \sqrt{LC} n'_{\text{eff}}} \quad (5)$$

where \sqrt{LC} is a constant (taking into account the described assumption) characteristic of the coil, and n'_{eff} is the real part of the effective refraction index $n'_{\text{eff}} = \sqrt{\mu'_{\text{eff}} \epsilon'_{\text{eff}}}$, which considers the contribution of all the materials around the coil.

Determining the effective refraction index of a composite medium is a complex problem explored in detail in the effective medium theory (EMT) [22]. In this context, the volume distribution of materials, their properties, and the electromagnetic field's spatial distribution determines the effective values of electrical permittivity and magnetic permeability. Given the high complexity, we need some simplification to provide a compact expression. For this purpose, we selected Lichtenecker's model [23,24], which provides enough accuracy to model the effective refraction index near our sensor with the required simplicity.

Instead of mathematically modelling the sample on top of our sensor realistically as a prism, we modelled it as a uniform mass distribution surrounding the coil track, as shown in Figure 3. In the figure, the NPs are represented as brown dots, and the matrix material as blue dots. On the left, we can see the NPs mingled with the matrix in the shape of a prism, whereas the same amounts of both materials are spread around the coil in the right figure, as used in mathematics.

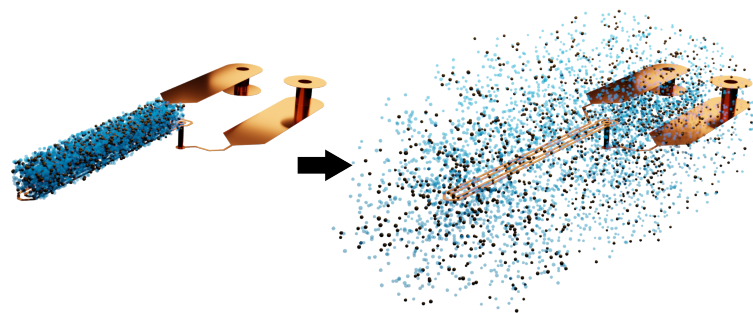


Figure 3. (Left) schematic representation of the sample (NPs and their embedding matrix) on top of the planar coil (here, the surrounding electronics and materials are not depicted) as used in experimental measurements and simulations; (right) scheme of the uniform particle distribution surrounding the coil as used in the mathematical model, with the same NPs and matrix amounts.

In this way, using Lichtenecker's logarithmic mixing formula, one can model the effective magnetic permeability and the effective electric permittivity with two formally identical expressions,

$$\ln(\mu_{\text{eff}}) = f \ln(\mu_s) + (1 - f) \ln(\mu_{\text{env}}) \quad (6)$$

$$\ln(\varepsilon_{\text{eff}}) = f \ln(\varepsilon_s) + (1 - f) \ln(\varepsilon_{\text{env}}) \quad (7)$$

which enables further simplification, as will be shown in the next section. Here, f is the volume fraction occupied by the sample concerning the volume where the magnitude of the electromagnetic field is larger than a given threshold; μ_{eff} and ε_{eff} are the effective permeability and permittivity, respectively, determined from the values μ_s and ε_s corresponding to the sample, and μ_{env} and ε_{env} for the environment. In turn, μ_s and ε_s are related to the mass of nanotags and their support.

Using the logarithmic Lichtenecker's mixing formula again results in

$$\ln(\mu_s) = \left(\left(\frac{m_{\text{NPs}}}{m_{\text{max}}} \right) \ln(\mu_{\text{NPs}}) \right) + \left(\left(1 - \left(\frac{m_{\text{NPs}}}{m_{\text{max}}} \right) \right) \ln(\mu_{\text{mtx}}) \right) \quad (8)$$

$$\ln(\varepsilon_s) = \left(\left(\frac{m_{\text{NPs}}}{m_{\text{max}}} \right) \ln(\varepsilon_{\text{NPs}}) \right) + \left(\left(1 - \left(\frac{m_{\text{NPs}}}{m_{\text{max}}} \right) \right) \ln(\varepsilon_{\text{mtx}}) \right) \quad (9)$$

As the NPs and the support are incompressible, $m_{\text{NPs}}/m_{\text{max}}$ is the volumetric relation, expressed as the ratio of NP mass in the sample and a reference mass corresponding to the same volume filled by NPs, with no voids; μ_{NPs} , ε_{NPs} , μ_{mtx} , and ε_{mtx} are the values of the magnetic permeability and electric permittivity of the NPs and the matrix, respectively.

Depending on the measurement procedure, there may be no matrix, but NPs are deposited on a sample holder or directly on the sensing element. The combined environment refraction index accounts for the sample support and matrix, $n_{\text{mtx}} = 1$. Using this

simplification and combining Equations (6)–(9), we obtain the following effective refraction index:

$$n_{\text{eff}} = n_{\text{env}} \left(\frac{n_{\text{NPs}}}{n_{\text{env}}} \right)^{f \left(\frac{m_{\text{NPs}}}{m_{\text{max}}} \right)} \quad (10)$$

Substituting n_{eff} in Equation (5) leads to a final expression that correlates the SRF to the mass of NPs in the sample as follows:

$$\text{SRF} = \frac{1}{2\pi n'_{\text{env}} \sqrt{LC} \left(\frac{n'_{\text{NPs}}}{n'_{\text{env}}} \right)^{\frac{f m_{\text{NPs}}}{m_{\text{max}}}}} \quad (11)$$

Using natural logarithms, expression (11) leads to

$$\ln(\text{SRF}) = m_{\text{NPs}} A_1 - A_0 \quad (12)$$

where

$$A_1 = - \frac{f}{m_{\text{max}}} \ln \left(\frac{n'_{\text{NPs}}}{n'_{\text{env}}} \right) \quad (13)$$

$$A_0 = \ln(2\pi \sqrt{LC} n'_{\text{env}}) \quad (14)$$

One needs to remark that A_1 is a function of the relative relation between the NPs (n'_{NPs}) and their environment (n'_{env}), while A_0 depends on the characteristics of the coil (LC) and the environment. In this way, we can calibrate any sensor by determining A_1 and A_0 through a linear fit of the law in (12) using several NP masses and the corresponding experimental SRFs. This calibration allows us to quantify unknown NP masses in the same device. As our sensor sensitivity is determined by the ratio between the effective refractive indexes of the sample and the environment, we defined this method as “refractometry sensing at radio-frequency”.

3. Simulation and Experimental Procedures

The mathematical model obtained from the targeted hypothesis needs verification. We sought to corroborate the working principle of radio-frequency refractometry, the validity of the hypothesis, and the real use of the model. The working principle and corroboration of the hypothesis are better tested using simulation in which we have absolute control over the defining measuring parameters, and it is possible to test situations that are not feasible with experimental techniques. For measurements, we developed an affordable testing rig to measure different types of NPs.

3.1. Simulation Setup

For the simulation of the sensing principle, we used a commercial finite element analysis tool, Ansys HFSS. Based on the geometry of the sensing setup and the electromagnetic properties of the materials, we extracted the impedance of the planar coil. The impedance was computed for a wide range of frequencies to find the first SRF point, which is the key value. The coil had two turns of 150 μm track width and separation and a length of 12 mm. The sample was a cuboid of 5 mm \times 1 mm \times 0.25 mm. The geometry of the planar circuit and sample are schematically shown in Figure 3 (left). We used a lumped port model to excite the planar inductor. The coil’s material was copper, whose properties were included in the simulation. The environment was introduced with arbitrary magnetic permeability and electric permittivity, which could be adjusted, and the sample with its electromagnetic properties. The boundary of the simulation perfectly absorbed the incident radiation-removing reflections. All simulations were performed with 1000 frequency points in a linear range between 0 and 3 GHz.

3.2. Experimental Setup

We performed the experimental measurements using a NanoVNA V2 calibrated at the end of the connection cables and derived the equivalent impedance of the coil from the scattering parameters. We made a linear interpolation between the first couple of positive and negative imaginary impedance values from the coil's impedance to extract the SRF. This impedance was measured with 1000 frequency points in a linear from 100 kHz to 3 GHz. The design of the sensor produced for testing matched the geometry of the simulated one, as shown in Figure 4, in which one can also see an adapter connecting it to NanoVNA V2.

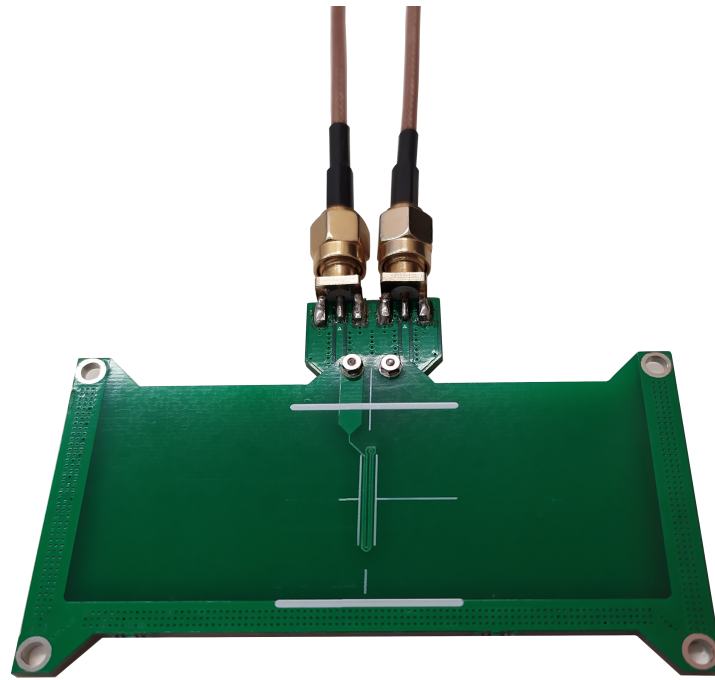


Figure 4. Adapter and planar coil on the printed circuit board used for the experimental measurements.

3.3. Nanoparticles for Testing

We used two materials to test the behaviour observed in the simulations: superparamagnetic magnetite and gold colloidal suspensions. We chose Fe_3O_4 due to its high magnetic permeability and electric permittivity. The suspensions were chemically synthesised by co-precipitating Fe(II/III) salts. This route is one of the most straightforward synthesis methods to obtain large amounts of magnetic material. Briefly, a 100 mL solution of 27% (*w/v*) of Fe(III) was prepared in a beaker. Consecutively, 12.94 g of Fe(II) were dissolved in 45 mL of the total volume in a graduated cylinder. A few drops of 37% HCl were added to both solutions to ensure the perfect dissolution of the salts and avoid the possible oxidation of iron cations. Then, both solutions were mixed and stirred vigorously. For the NPs to precipitate, a basic solution was added. The drastic change in pH allows the nucleation and growth of the NPs. To have some control of these two processes, the precipitating agent must be added slowly. Therefore, a solution of 75 mL of 25% ammonia was slowly poured. Finally, the NPs obtained were magnetically decanted to eliminate the residues of the reaction three times. Then, the NPs were resuspended in distilled water.

The average NP size was 12 nm. The permeability and permittivity values of these MNPs were not measured. Still, similar ones appeared in the literature [25,26] presenting values of the relative permeability μ'_{MNPs} at RF between 1.5 and 2 and relative electric permittivity ϵ'_{MNPs} between 6 and 8. The gold NPs were a commercial colloid of spherical particles with a diameter of 5.6 nm. Their electric permittivity was not measured, but some studies [27] report ϵ'_{GNPs} values between 1.5 and 3 in similar particles. The NPs were

deposited on blotting paper using a custom printer that drops a controlled flow of solution along a line pattern. Printing was performed with a flow of $3.03 \mu\text{L}/\text{s}$ at a speed of $33 \text{ mm}/\text{s}$. All the blotting paper pieces had the same dimensions $80 \text{ mm} \times 25 \text{ mm}$, and their shape was determined to provide a uniform pressure distribution on the sensor. The shape of the lines of deposited NPs was a rectangle of $25 \text{ mm} \times 2 \text{ mm}$. Figure 5 shows the pictures of some of the tested samples.

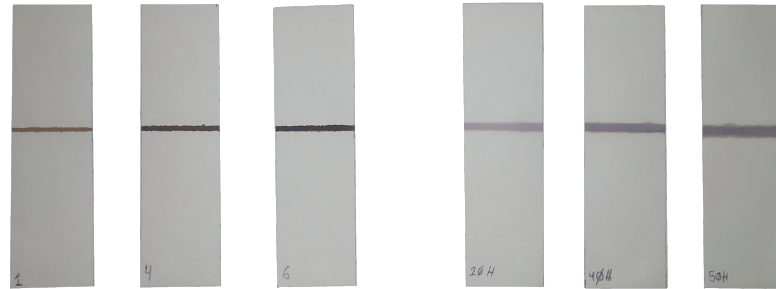


Figure 5. (Left) some magnetite NP samples; (right) some gold NPs samples. In all cases, NPs were deposited on blotting paper and placed on the sensing coil in the experimental setup.

The blotting paper had to be flattened against the sensing surface to eliminate ripples, thus helping to keep the NP deposition at the same distance in every measurement. We achieved this by applying pressure onto the blotting paper. The clamping force, which compresses the paper, impacts the environment's refraction index. Keeping it constant between measurements is critical to improving repeatability. For this purpose, we fabricated a custom sample holder to fix the samples firmly on top of the sensing coil. The sample holder had a plunger through which pressure was applied on both sides of a Teflon plate on top of the sensing area. The symmetric pressure resulted in a uniform tension distribution on the plate and, thus, a repeatable and predictable contact. To ensure this tension distribution, we used a 4-bar mechanism that kept the symmetric plunger parallel to the sensing circuit board. The pressure jig is shown in Figure 6.

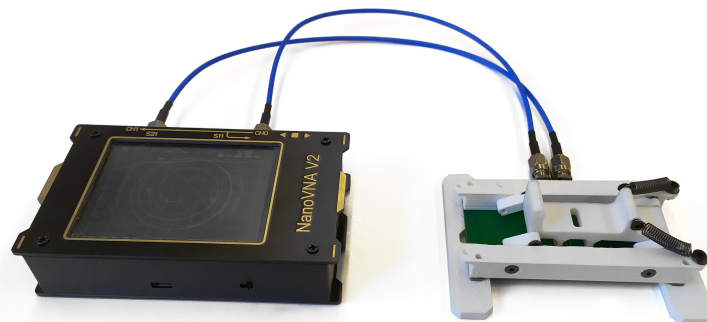


Figure 6. Pressure jig in combination with NanoVNA V2.

4. Results and Discussion

4.1. Simulation Results

First, we tested the sensitivity of the simulated setup with different ideal NPs to verify the importance of the electric permittivity and its impact on the drift of the coil's SRF. Specifically, the following parameter values were used: $\mu_{\text{NPs}} = 1$, $\epsilon_{\text{NPs}} = 10$; $\mu_{\text{NPs}} = 10$, $\epsilon_{\text{NPs}} = 1$; and $\mu_{\text{NPs}} = \epsilon_{\text{NPs}} = 10$.

Figure 7 shows the dependence of the $\ln(\text{SRF})$ on the ratio $m_{\text{NP}}/m_{\text{max}}$ for the NPs in all three cases.

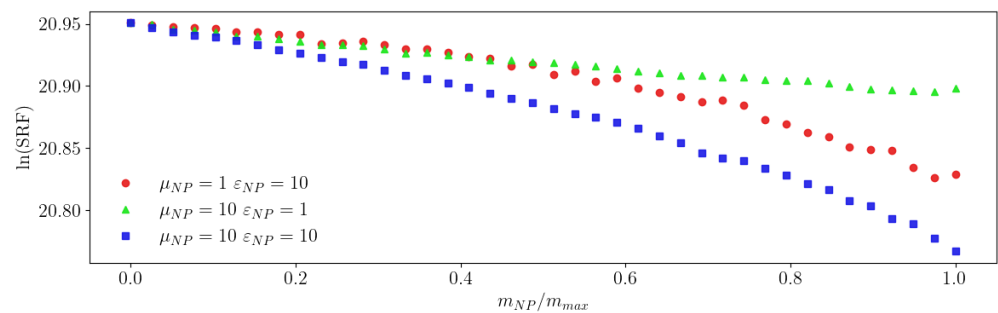


Figure 7. Dependence of the $\ln(\text{SRF})$ on the ratio $m_{\text{NP}}/m_{\text{max}}$ for the simulated NPs.

With these simulation parameters, 0% mass yielded $\ln(\text{SRF}) = 20.95$. When only the electric permittivity (red circles in Figure 7) or the magnetic permeability (green triangles) were increased from their minimum unity value, the $\ln(\text{SRF})$ monotonically decreased in the same way, as can be seen with the superposition of the two curves until 50% of mass ratio. This result proves that, as long as the refraction index was the same, regardless of whether it was μ_{NPs} or ϵ_{NPs} that would change, the $\ln(\text{SRF})$ evolved in the same way as the NP mass. When the refraction index increased, as in the curve with blue squares (Figure 7), the decrease in the $\ln(\text{SRF})$ with the mass was accentuated. This simulation behaviour is consistent with our mathematical model as long as the variation in $\ln(\text{SRF})$ was less than 0.04, which corresponds to an SRF change of approximately 50 MHz (here, a mass ratio of 50%). This maximum variation in the SRF depends on the specific sensing coil, the environment, and NP properties. Under this limitation, the signal's response is linear versus the mass, and the slope follows Equation (13). These results prove that inductive sensors, working in their SRF point, are sensitive to both magnetic permeability and electric permittivity and, for small variations in the SRF (such as those produced with small amounts of NPs), are well described using the mathematical model presented in this article. Consequently, the method can be used to take advantage of the inductive and capacitive effects in the coil to detect NPs with increased sensitivity.

One of this work's most significant simplifying assumptions is the dismissal of the imaginary parts of the magnetic permeability and the electric permittivity. To check the impact of this simplification, we simulated the system in the presence of different NPs, specifically with loss tangents of $\tan(\delta_e) = \tan(\delta_m) = 0$, $\tan(\delta_e) = \tan(\delta_m) = 0.05$, and $\tan(\delta_e) = \tan(\delta_m) = 0.1$, where $\delta_m = \mu''/\mu'$ and $\delta_e = \epsilon''/\epsilon'$.

Figure 8 shows that there is no effect of μ'' and ϵ'' on the sensor response for a sample with $\mu_{\text{NP}}' = \epsilon_{\text{NP}}' = 10$. This allows us to conclude that neglecting the imaginary parts of μ and ϵ is an acceptable assumption.

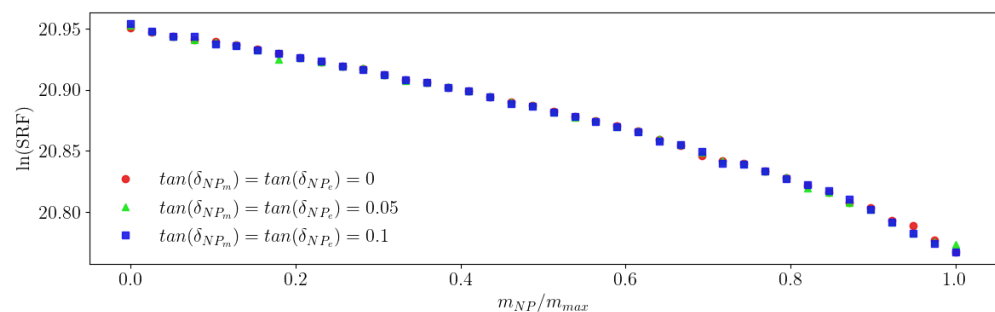


Figure 8. Dependence of the $\ln(\text{SRF})$ on the ratio $m_{\text{NP}}/m_{\text{max}}$ for different lossy NPs.

The following simulation focuses on the environment's effect. Manufacturing an actual sensor involves using materials whose refraction index significantly influences its behaviour. We performed simulations with the expected values of the environment

permeabilities and permittivities in three cases: when the coil is in vacuum, $\mu_{\text{env}} = \epsilon_{\text{env}} = 1$; for the coil on top of a fibreglass material, for which we assumed $\mu_{\text{env}} = 1$ and $\epsilon_{\text{env}} = 3$; and if the sensor is surrounded by fibreglass, we used $\mu_{\text{env}} = 1$ and $\epsilon_{\text{env}} = 4$. In all cases, we assumed that no ferro- or ferri-magnetic material, apart from the sample, was near the coil.

For the simulation with the same NP parameters as before, $\mu_{\text{NPs}} = \epsilon_{\text{NPs}} = 10$, we obtained the results shown in Figure 9.

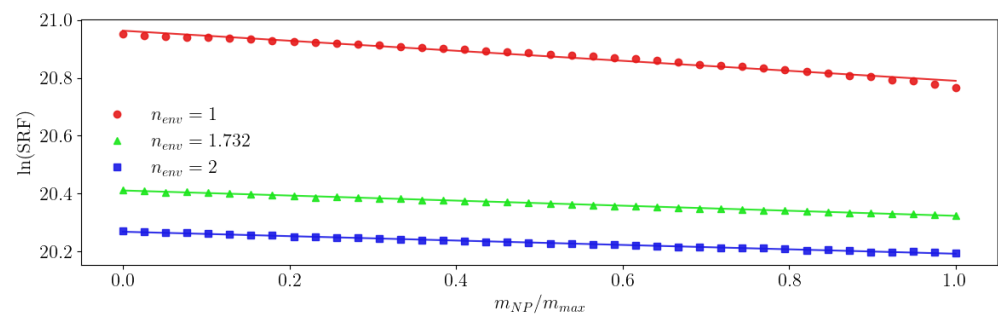


Figure 9. Dependence of the $\ln(\text{SRF})$ on the ratio $m_{\text{NP}}/m_{\text{max}}$ for several environment refraction indexes. The solid lines are their fitness to our model (12).

Using Equation (12), we fitted the simulated data in all three cases, thus obtaining the parameters shown in Table 1.

Table 1. Fitting to Equation (12) of the simulation results for several refraction indexes in the environment.

	A_1	A_0	R^2
$n_{\text{env}} = 1$	-1.7313×10^{-1}	-20.9629	0.9776
$n_{\text{env}} = 1.732$	-8.7557×10^{-2}	-20.4109	0.9981
$n_{\text{env}} = 2$	-7.6000×10^{-2}	-20.2684	0.9940

In this simulation, the NPs were the same, so the differences in A_1 and A_0 values came exclusively from the variation in the environment's refraction index. Based on the R^2 values, it could be inferred that the model's validity was compromised when the difference between the environment and the NP refraction indexes significantly increased. This problem resulted from trying to accommodate large variations in the SRF against our model's premises. When n_{env} increases A_1 , the line slope's absolute value decreases, thus decreasing the sensitivity of the measurement.

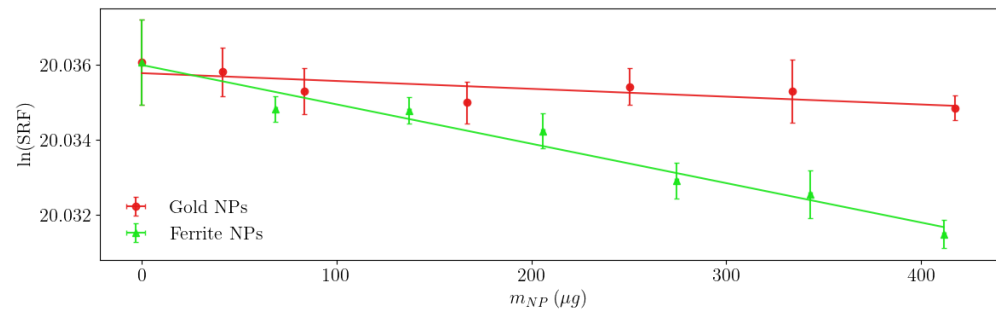
4.2. Experimental Results

Figure 10 shows the results of measuring gold (red circles) and magnetite (green triangles) NPs with our sensor to validate the mathematical model (12). The corresponding linear regression parameters are shown in Table 2.

We can observe some differences between the experimental (Table 2) and simulated (Table 1) A_0 values. This is due to the change in the LC product (see Equation (14)) associated with the coil geometry (more precisely to the adapter, which can be seen in Figure 4). Regardless, these results prove that, despite the low concentration of NPs, the magnetite NPs exhibit five times the signal of the gold ones, with the same mass. This is evidenced by the sensitivity values A_1 and easily explained by the higher refraction index of MNPs. This difference also explains the low R^2 value of the gold. This result validates our analysis of the sensor based on changes in the SRF and confirms the possibility of easily quantifying the MNP mass in a test sample.

Table 2. Fitting results of the experimental data.

	A_1	A_0	R^2
Gold NPs	-2.0871×10^{-6}	-20.0358	0.5815
Magnetite NPs	-1.0493×10^{-5}	-20.0360	0.9651

**Figure 10.** Measurements with the experimental setup (symbols) and model adjustment (lines).

Considering the significant differences between this method and previous ones using both the self-inductance and self-capacitance of the inductive sensor, even when the purpose of the study is not to optimise the sensor's characteristics but to evaluate the mathematical and measurement method, there is a remarkable improvement in the sensitivity S , which is multiplied by 1940, $S = 5821.4 \text{ Hz}/\mu\text{g Fe}_3\text{O}_4$ compared to $S = 3 \text{ Hz}/\mu\text{g Fe}_3\text{O}_4$ achieved in previously reported ones [9]. Even if we normalise the sensitivity by dividing it by the operating frequency in the absence of NPs, the improvement is 2.04 times. This also shows the importance of measuring at higher frequencies, which implies including the sensor's capacitive effects and the sample's electric permittivity.

5. Conclusions

Inductive sensors are affected by their environment's electric permittivity and magnetic permeability. The importance of both factors increases as the working frequency approaches the coil's SRF. For this reason, measuring the SRF of the sensing coil in the presence of NPs can be used to quantify them with increased sensitivity. The refraction index ratio between NPs and the whole environment determines the sensor sensitivity. In the case of MNPs, their higher magnetic permeability leads to better sensitivity, as it increases the refraction index ratio $n_{\text{NPs}}/n_{\text{env}}$.

In this work, we established some hypotheses under which our sensor exhibits a linear regime. This idea allowed us to calibrate the sensor using a linear fit from a sample set of known masses. This approach is limited to low-loss samples and small variations in the SRF. Using the coil's SRF combined with our mathematical model opens the way to develop an affordable, portable, and reliable sensor to detect and quantify small numbers of MNPs. In future works, for example, it can be applied to develop an optimised magnetic lateral-flow immunoassay reader that provides qualitative and quantitative results without compromising the main advantages of rapid paper tests.

Author Contributions: Conceptualisation, J.L.M.-F., J.C.M.-G., P.F.-M. and M.R.; data curation, J.L.M.-F., M.S., J.C.M.-G. and M.R.; formal analysis, J.L.M.-F., M.S., J.C.M.-G., P.F.-M., A.G.-A. and M.R.; funding acquisition, J.C.M.-G. and M.R.; investigation, J.L.M.-F., J.C.M.-G. and M.R.; methodology, J.L.M.-F., M.S., J.C.M.-G. and M.R.; project administration, J.C.M.-G. and M.R.; resources, J.L.M.-F., M.S., J.C.M.-G., P.F.-M., A.G.-A. and M.R.; software, J.L.M.-F.; supervision, J.C.M.-G. and M.R.; validation, J.L.M.-F., M.S., J.C.M.-G., A.G.-A. and M.R.; visualisation, J.C.M.-G. and M.R.; writing—original draft preparation, J.L.M.-F. and J.C.M.-G.; writing—review and editing, J.L.M.-F., M.S., J.C.M.-G., P.F.-M., A.G.-A. and M.R. All authors have read and agreed to the published version of the manuscript.

Funding: This work was partially founded by the Ministry of Science and Innovation of the Spanish Government through grant PLEC2022-009490, the University Technological Institute of Asturias (IUTA), under grant SV-22-GIJON-18, and the Government of the Principality of Asturias under projects FICYT/IDI/2021/000100 and FICYT/IDI/2021/000273. M.S. was supported by a “Severo Ochoa” fellowship (Consejería de Educación y Cultura del Gobierno del Principado de Asturias, grant BP19-141) and by the Margarita Salas fellowship financed by the European Union-NextGenerationEU and the Plan for Recovery, Transformation and Resilience.

Institutional Review Board Statement: Not applicable.

Informed Consent Statement: Not applicable.

Data Availability Statement: Not applicable.

Acknowledgments: We thank Ron B. Goldfarb (NIST) for insightful discussions and Javier F. Sebastián for providing technical and human resources to ease the prototype development.

Conflicts of Interest: The authors declare no conflict of interest. The funders had no role in the design of the study; in the collection, analyses, or interpretation of data; in the writing of the manuscript; or in the decision to publish the results.

Abbreviations

The following abbreviations are used in this manuscript:

SRF	Self-resonant frequency
MNPs	Magnetic nanoparticles
NPs	Nanoparticles

References

1. Salvador, M.; Martínez-García, J.; Fernández-García, M.; Blanco-López, M.C.; Rivas, M. Biological and Medical Applications of Magnetic Nanoparticles. In *Magnetic Measurement Techniques for Materials Characterization*; Springer: Cham, Switzerland, 2021; pp. 771–804. [[CrossRef](#)]
2. Yamada, K.; Shibata, H.; Suzuki, K.; Citterio, D. Toward practical application of paper-based microfluidics for medical diagnostics: State-of-the-art and challenges. *Lab Chip* **2017**, *17*, 1206–1249. [[CrossRef](#)] [[PubMed](#)]
3. Banerjee, R.; Jaiswal, A. Recent Advances in Nanoparticle-based Lateral Flow Immunoassay as a Point of Care Diagnostic Tool for Infectious Agents and Diseases. *Analyst* **2018**, *143*, 1970–1996. [[CrossRef](#)]
4. Parolo, C.; Sena-Torralla, A.; Bergua, J.F.; Calucho, E.; Fuentes-Chust, C.; Hu, L.; Rivas, L.; Álvarez-Diduk, R.; Nguyen, E.P.; Cinti, S.; et al. Tutorial: Design and fabrication of nanoparticle-based lateral-flow immunoassays. *Nat. Protoc.* **2020**, *15*, 3788–3816. [[CrossRef](#)]
5. Liu, C.; Jia, Q.; Yang, C.; Qiao, R.; Jing, L.; Wang, L.; Xu, C.; Gao, M. Lateral Flow Immunochromatographic Assay for Sensitive Pesticide Detection by Using Fe₃O₄ Nanoparticle Aggregates as Color Reagents. *Anal. Chem.* **2011**, *83*, 6778–6784. [[CrossRef](#)] [[PubMed](#)]
6. Poonlapdech, W.; Seetang-Nun, Y.; Wonglumsom, W.; Tuitemwong, K.; Erickson, L.E.; Hansen, R.R.; Tuitemwong, P. Antibody-conjugated ferromagnetic nanoparticles with lateral flow test strip assay for rapid detection of *Campylobacter jejuni* in poultry samples. *Int. J. Food Microbiol.* **2018**, *286*, 6–14. [[CrossRef](#)] [[PubMed](#)]
7. Razo, S.C.; Panferov, V.G.; Safenkova, I.V.; Varitsev, Y.A.; Zherdev, A.V.; Dzantiev, B.B. Double-enhanced lateral flow immunoassay for potato virus X based on a combination of magnetic and gold nanoparticles. *Anal. Chim. Acta* **2018**, *1007*, 50–60. [[CrossRef](#)]
8. Moyano, A.; Serrano-Pertierra, E.; Salvador, M.; Martínez-García, J.; Rivas, M.; Blanco-López, M.C. Magnetic Lateral Flow Immunoassays. *Diagnostics* **2020**, *10*, 288. [[CrossRef](#)]
9. Richardson, J.; Hill, A.; Luxton, R.; Hawkins, P. A novel measuring system for the determination of paramagnetic particle labels for use in magneto-immunoassays. *Biosens. Bioelectron.* **2001**, *16*, 1127–1132. [[CrossRef](#)]
10. Lago-Cachón, D.; Rivas, M.; Martínez-García, J.; García, J. Cu impedance-based detection of superparamagnetic nanoparticles. *Nanotechnology* **2013**, *24*, 245501. [[CrossRef](#)]
11. Rivas, M.; Lago-Cachón, D.; Martínez-García, J.; García, J.; Calleja, A. Eddy-current sensing of superparamagnetic nanoparticles with spiral-like copper circuits. *Sens. Actuators A Phys.* **2014**, *216*, 123–127. [[CrossRef](#)]
12. Lago-Cachón, D.; Rivas, M.; Martínez-García, J.; Oliveira-Rodríguez, M.; Blanco-López, M.; García, J. High frequency lateral flow affinity assay using superparamagnetic nanoparticles. *J. Magn. Magn. Mater.* **2017**, *423*, 436–440. [[CrossRef](#)]
13. García-Arribas, A. The Performance of the Magneto-Impedance Effect for the Detection of Superparamagnetic Particles. *Sensors* **2020**, *20*, 1961. [[CrossRef](#)]
14. Barnett, J.M.; Wraith, P.; Kiely, J.; Persad, R.; Hurley, K.; Hawkins, P.; Luxton, R. An Inexpensive, Fast and Sensitive Quantitative Lateral Flow Magneto-Immunoassay for Total Prostate Specific Antigen. *Biosensors* **2014**, *4*, 204–220. [[CrossRef](#)] [[PubMed](#)]

15. Lago-Cachón, D.; Oliveira-Rodríguez, M.; Rivas, M.; Blanco-López, M.C.; Martínez-García, J.C.; Moyano, A.; Salvador, M.; García, J.A. Scanning Magneto-Inductive Sensor for Quantitative Assay of Prostate-Specific Antigen. *IEEE Magn. Lett.* **2017**, *8*, 1–5. [[CrossRef](#)]
16. Okada, K.; Masu, K. Modeling of Spiral Inductors. *Adv. Microw. Circuits Syst.* **2010**, *4*, 291–312. [[CrossRef](#)]
17. Collier, R. *Transmission Lines: Equivalent Circuits, Electromagnetic Theory, and Photons*; Cambridge RF and Microwave Engineering Series; Cambridge University Press: Cambridge, UK, 2013.
18. Heathcote, M. *The J & P Transformer Book: A Practical Technology of the Power Transformer*; Newnes: Oxford, UK, 2007.
19. Bartoli, M.; Reatti, A.; Kazimierczuk, M. Modelling iron-powder inductors at high frequencies. In Proceedings of the 1994 IEEE Industry Applications Society Annual Meeting, Denver, CO, USA, 2–6 October 1994; Volume 2, pp. 1225–1232. [[CrossRef](#)]
20. Nomura, K.; Kojima, T.; Hattori, Y. Straightforward Modeling of Complex Permeability for Common Mode Chokes. *IEEE J. Ind. Appl.* **2018**, *7*, 462–472. [[CrossRef](#)]
21. Yu, Q.; Holmes, T.; Naishadham, K. RF equivalent circuit modeling of ferrite-core inductors and characterization of core materials. *Electromagn. Compat. IEEE Trans.* **2002**, *44*, 258–262. [[CrossRef](#)]
22. Wang, M.; Pan, N. Predictions of effective physical properties of complex multiphase materials. *Mater. Sci. Eng. R Rep.* **2008**, *63*, 1–30. [[CrossRef](#)]
23. Goncharenko, A.; Lozovski, V.; Venger, E. Lichtenecker’s Equation: Applicability and Limitations. *Opt. Commun.* **2000**, *174*, 19–32. [[CrossRef](#)]
24. Zakri, T.; Laurent, J.P.; Vauclin, M. Theoretical Evidence for ‘Lichtenecker’s Mixture Formulae’ Based on the Effective Medium Theory. *J. Phys. D Appl. Phys.* **1999**, *31*, 1589. [[CrossRef](#)]
25. Hirose, Y.; Hasegawa, D.; Ohki, Y. Development of composite of epoxy resin and iron nanoparticles as a low eddy-current loss magnetic material. In Proceedings of the 2011 International Symposium on Electrical Insulating Materials, Kyoto, Japan, 6–10 September 2011; pp. 337–340. [[CrossRef](#)]
26. Scarlatache, V.A.; Olariu, M.; Ursache, S.; Ciobanu, R.C.; Pasquale, M. Magnetic and dielectric losses of a nanocomposites polymer matrix reinforced with ferromagnetic powders. In Proceedings of the 2012 International Conference and Exposition on Electrical and Power Engineering, Iasi, Romania, 25–27 October 2012; pp. 125–128. [[CrossRef](#)]
27. Abdelhalim, M.A.K.; Mady, M.M.; Ghannam, M.M. Rheological and dielectric properties of different gold nanoparticle sizes. *Lipids Health Dis.* **2011**, *10*, 208. [[CrossRef](#)] [[PubMed](#)]

Disclaimer/Publisher’s Note: The statements, opinions and data contained in all publications are solely those of the individual author(s) and contributor(s) and not of MDPI and/or the editor(s). MDPI and/or the editor(s) disclaim responsibility for any injury to people or property resulting from any ideas, methods, instructions or products referred to in the content.